

A Bionic Piezoelectric Robotic Jellyfish with a Large Deformation Flexure Hinge

Jichun Xing, *Membership, IEEE*, Wei Jin, Kuang Yang, and Ian Howard

Abstract—Jellyfish are one of the underwater creatures that have been imitated by underwater bionic robots, but a current challenge to create a bionic jellyfish is with the use of piezoelectric ceramic sheets as the driving element, due to their small output displacement. Here, a bionic robotic jellyfish with three tentacles is presented that is driven by three piezoelectric beams, and to transmit power, a large deformation composite flexure hinge is created which employs fishing line embedded in a 3D printed structure. In addition, the structure design and fabrication of the drive system are described. A dynamic model of the drive system is established to solve for the working mode, forced displacement responses, and swimming lift. A series of experiments are carried out to verify the theoretical analysis and validate the design of the robotic jellyfish. The proposed robotic jellyfish has a total mass of 29.4 g, tentacle spread of about 150 mm, and an overall height of 100 mm. The robotic jellyfish can exhibit swimming performance with drive frequencies of 0.7-1.1 Hz, and the best achieved swimming speed was 10 mm/s. These design, modeling, and fabrication methods may be beneficial and inspiring for the future development of the micro soft robot.

Index Terms—Robotic jellyfish, Piezoelectric drive, Flexure hinge, Soft robot.

I. INTRODUCTION

Human exploration of the ocean promotes the development of underwater robots. The application of underwater robots involves environmental surveys, water quality monitoring, seabed and abyssal exploration, aquatic species monitoring and data collection [1]. To improve their environmental compatibility and interaction safety concerns, researchers have a great interest in the development of bionic robots mimicking the locomotion of underwater creatures. Jellyfish are typical of the underwater creatures that have inspired researchers to create bionic underwater robots using various actuators [2, 3]. For the driving modes of bionic jellyfish robots, the conventional driving modes usually employ an electric, pneumatic, or hydraulic motor to drive flexible fins and torso for generating propulsion [4-7]. These rigid robots have limited flexibility and adaptability to their environment, and their designs can make it difficult to achieve an optimal

Manuscript received Month xx, 2022; revised Month xx, xxxx; accepted Month x, xxxx. (Corresponding author: Jichun Xing). This work was supported by State Key Laboratory of Robotics and System (HIT).

J.C. Xing, W. Jin and K. Yang are with the School of Mechanical Engineering, Yanshan University, Qinhuangdao, 066004, China, (e-mail: xingjichun@ysu.edu.cn, jin-wei@stumail.ysu.edu.cn, yangkuang20216@stumail.ysu.edu.cn).

I. Howard is with the School of Civil and Mechanical Engineering, Curtin University, Perth, 6102, Australia, (e-mail: I.Howard@exchange.curtin.edu.au).

swimming motion. However, the development of smart materials brings an opportunity for exploration and attempt to replace the rigid actuation and transmission components with soft actuation to offer more adaptability. The application of smart materials endows new properties of underwater robots in miniaturization, intelligence, and integration [8]. The typical soft actuation technologies for robotic jellyfish can be summarized as thermally responsive actuators, magnetically responsive actuators, and electrically responsive actuators [9].

Thermally responsive materials used in underwater robots include shape memory alloy (SMA) [10, 11], and twisted and coiled polymer (TCP) muscles [12]. For example, Villanueva et al. presented a robotic jellyfish that actuates using bio-inspired shape memory alloy composite actuators and was fabricated from silicone [13]; Hamidi et al. created two kinds of bio-inspired jellyfish robots, named KryptoJelly and Poly-Saora, which were fabricated by SMA and TCP actuators separately [14]. However, the performance of the bionic robots with thermally responsive actuators is impacted by the water temperature in some way.

Magnetically responsive materials used in underwater robots can be innovatively integrated and embedded in the robot body and has been widely applied in untethered microrobots, but the magnetic field in space limits its range of motion [15]. Ko et al. proposed a jellyfish-like swimming mini-robot driven by the electromagnetic actuation (EMA) method. The mini-robot had four flexible fins with a permanent magnet for EMA and was able to perform 3D swimming motions [16]. Ren et al. proposed an untethered jellyfish-inspired soft millirobot that could produce diverse controlled fluidic flows around its body to float upward and downward by using its magnetic composite elastomer lappets [17].

Electrically responsive materials subject to an electric field are able to deform. The representative materials are ionic polymer metal composites (IPMC) [18] and dielectric elastomers (DE) [19] and piezoelectric materials [20]. IPMC actuators can generate high flexural strains. Given this, many researchers have devised underwater Jellyfish-like robots using IPMC as propulsion actuators [21, 22]. Rather than the low response of IPMC, the DE have high compliance and fast response. Wang et al. exhibited a developed jellyfish robot that combines a dielectric elastomer diaphragm actuator with a transmission mechanism [23]. Christianson et al. developed an untethered soft robot powered by DEAs, which attached a ring of frameless DEAs to an inextensible layer to generate a unimorph structure [24]. However, voltages of several thousand volts are required to operate DEAs. Piezoelectric materials with the characteristics of fast response and relatively moderate driving voltage, such as Polyvinylidene fluoride (PVDF),

Macro fiber composite (MFC), and Piezoelectric ceramics (PZT), have usually been employed to fabricate various actuators and bionic robots [25-28], though fewer have been used in jellyfish-like robots [29]. Among piezoelectric materials, piezoelectric ceramics have the fastest response speed, the lowest driving power, and the highest energy density. However, due to the small deformation, it is difficult to fabricate bionic jellyfish with piezoelectric ceramics. To transmit and amplify the displacement of piezoelectric actuators, Wood et al. created a large deformation flexure hinge which was formed by carbon fiber and polyimide film, and developed several kinds of micro robots [30, 31]. The small bending stiffness of this micron-scale flexible hinge can fabricate sub-centimeter-scale microrobots (e.g., RoboBees). However, such flexure hinges are not suitable for relatively large-size robotic jellyfish due to insufficient rigidity. Therefore, it is still a challenge to invent a novel type of flexure hinge with large deformation for a centimeter-scale miniature robot.

Inspired by this, to further expand the application scope of piezoelectric ceramics in soft bionic robots, the current paper proposes a large deformation flexure hinge made of fishing line embedded in 3D printing components to create a novel centimeter-scale bionic jellyfish. Three piezoelectric driving units with tentacle-like were arranged around the jellyfish's body and it could achieve a higher imitation of underwater creatures' swimming motion. The design scheme and fabrication processes of the robotic jellyfish are described in detail in Section II. The multi-continuum coupled dynamic equations and propulsion force of the jellyfish-like robot were established to determine the optimum drive frequency and working mode in Section III. A prototype of the proposed robotic jellyfish was manufactured to assess the motion characteristics under different excitations. Section IV presents the dynamic behaviors of the drive system that were measured to verify the theoretical analysis. Finally, the conclusion and prospects are introduced in Section V.

II. DESIGN AND FABRICATION

A. Configuration of the robotic jellyfish

The proposed bionic robotic jellyfish has three tentacles that are evenly distributed around the jellyfish body. These take up the power of the piezoelectric drive beams to push water for swimming with the recoil principle. The output displacement of the piezoelectric beam is amplified to supply the tentacles by a flexible amplification mechanism (FAM), as seen in Fig. 1(a) and (c). Therefore, the piezoelectric beams, FAM, and tentacles form the core components of the drive systems. The piezoelectric drive beams are composed of a brass beam as substrate and two piezoelectric sheets (PZT-5H $40 \times 10 \times 0.23$ mm). The propulsion tentacles are made of carbon fiber to enhance the adaptation. The movements of the robotic jellyfish come close to the biological role model. The FAM is manufactured by 3D printing with Polylactic Acid (PLA) material. During the printing process, two strands of the fishing line (Nylon 6, $R = 0.28$ mm) are embedded into the model as the flexure hinge. The reserved grooves of the FAM are employed to connect the piezoelectric beam and the tentacle

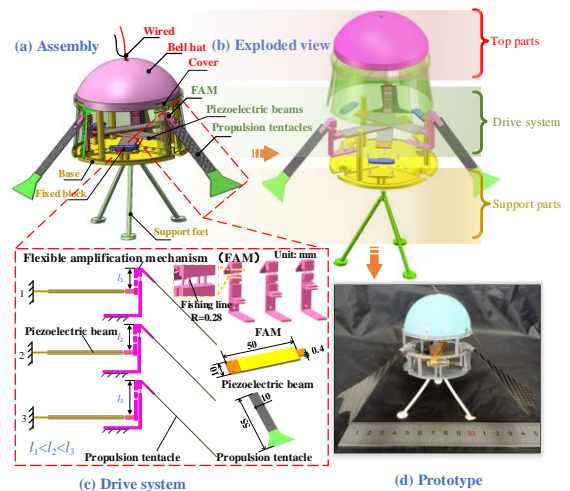


Fig. 1. The configuration of the bionic robotic jellyfish. (a) robotic jellyfish assembly; (b) exploded view; (c) drive system; (d) the prototype.

(see Fig. 1(c)). To create a compact structure, the three sets of drive parts are arranged on top of each other at a certain distance in the vertical direction and 120° apart. Therefore, while ensuring the same height of the output end of the FAMs, to avoid the interference of the piezoelectric beams, the different heights of the input ends of the three sets of the FAMs are designed, as shown in Fig. 1(c), e.g., $l_1 < l_2 < l_3$. The FAMs and one end of the piezoelectric beams are fixed on the base, and the support feet are mounted in the central hole of the base. The function of the feet can not only hold up the base, but also support some weights on the feet to balance the buoyancy. The base and support feet are attributed to support parts. A cover that provides space for the tentacles to stretch out is connected to the base to envelop the drive systems. The bell hat on the cover can reduce the resistance of the robotic jellyfish when swimming. The space of the bell hat is also able to be utilized to contain a balloon to provide buoyancy. The main parts of the robotic jellyfish are made by 3D printing and their materials are PLA. The cover and bell hat form the top parts (see Fig. 1(b)). The completed prototype of the robotic jellyfish is presented in Fig. 1(d). It has a total weight of 29.5 g, tentacles spread of about 150 mm, and an overall height of 100 mm.

B. Manufacturing process and working principle

The output of motion is attributed to the design and fabrication of the FAMs. The output of the piezoelectric beam needs a FAM with high flexibility and long life. It is hard to devise FAMs from single materials having large flexibility, high fatigue life of the flexure hinge with relatively high stiffness links in a small dimension. Here, we innovatively embed fishing line into the 3D printed components to produce a composite flexure hinge suitable for the transmission of motion and power of micro-robots.

The manufacturing process of the FAM is presented in Fig. 2(a). First, the model of FAMs with determined parameters is completed in 3D design software, and the spaces and holes for laying the fishing line are reserved. Then, the model data is input into a 3D printer and printed. Since a FAM has two strands of fishing line, when the printing process is 25% and 75 % finished, the 3D printer is paused. The fishing line is laid in the hole and fixed with glue. After that, the 3D printer is resumed and proceeded until completion. Lastly, the completed

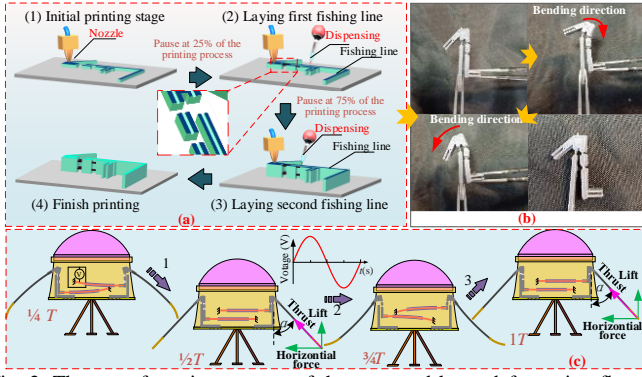


Fig. 2. The manufacturing process of the proposed large deformation flexure hinge and working principle of the robotic jellyfish. (a) manufacturing process; (b) demonstration; (c) working principle.

FAM is removed from the printer for final polishing. This type of flexure hinge with fishing line is capable of large-scale deformation under low force, as shown in Fig. 2 (b). Moreover, different topological arrangements (parallel, triangle, and cross) of fishing lines can create flexible hinge forms with different stiffnesses.

For the working principle of the drive system, the descriptions can be obtained from Fig. 2(c). When a sinusoidal drive signal is supplied into the piezoelectric beam, the piezoelectric beam generates downward bending in the first quarter cycle, while, the tentacle takes the power through the transmission of the FAM to push the water up. During $(1/4)T$ to $(3/4)T$, the voltage drops and changes direction then increases. The piezoelectric beam restores the deformation and generates upward bending. In this process, the tentacle pushes the water down. After $(3/4)T$, the negative voltage of the drive signal decreases, and the piezoelectric beam restores the deformation and the tentacle pushes the water up. Due to the angle α between the tentacles and the vertical direction, the vertical component of the thrust of the fluctuating water by the three tentacles causes the jellyfish to swim upward.

III. DYNAMICS BEHAVIOR ANALYSIS OF THE DRIVE SYSTEM

The propulsion force is a core indicator for the performance of robotic jellyfish. Its solution requires the underwater dynamic response displacement of the tentacle to be calculated. According to the research results of Sader [32], the additional mass and damping caused by the viscous fluid can be considered and introduced into the dynamic equation of the beam without water to calculate the underwater dynamic response of the beam. So, the free and forced vibration analysis for the drive system without water are to be completed initially.

A. Free vibration analysis for the drive system without water

For the solution of the modal function and natural frequency of the drive system, the physical model is simplified as shown in Fig. 3(a). Since the FAM includes multiple flexure hinges, here, the overall stiffness of a flat coil spring is obtained, having contributions from all flexure hinges. The connection between the FAM and tentacle is also considered a transition beam. Due to the output of the piezoelectric beam being sub-millimeter scale and the defamation of each flexure hinge being small, the pseudo-stiffness method is employed to analyze the geometric

relationship of motion as shown in Fig. 3(b). The distances between the flexure hinges are denoted by S_i , the output of the piezoelectric beam is denoted by x_a . According to the geometric relationship, the rotation angle of the transition beam can be approximated as $\theta_3 \approx x_a/S_3$. Each sub-system of the beams is considered as an Euler–Bernoulli beam. The functions $w_1(x_1, t)$, $w_2(x_2, t)$, $w_3(x_3, t)$ represent the longitude displacement of the piezoelectric beam, transition beam, and tentacle separately, and l_i ($i=1, 2, 3$) represents the length of the piezoelectric beam, transition beam, and tentacle separately. l_{20} is the distance between the joint of the piezoelectric beam and the rotation center of the transition beam, which belongs to the transition beam during the calculation.

For the dynamic equation of the piezoelectric beam, according to the dynamics method of continuous systems, we have

$$E_b I_1 \frac{\partial^4 w_1(x_1, t)}{\partial x_1^4} + m_1 \frac{\partial^2 w_1(x_1, t)}{\partial t^2} = 0 \quad (1)$$

where $E_b I_1$ is the bending stiffness of the piezoelectric composite beam, m_1 is the mass per unit length of the piezoelectric composite beam. Let the solution of Eq. (1) be

$$w_1(x_1, t) = \phi_1(x_1) q_1(t) \quad (2)$$

where $\phi_1(x_1)$ is the modal function of the piezoelectric beam, $q_1(t)$ is the generalized coordinates. Substituting Eq. (2) into Eq. (1), the equation for the modal function can be obtained

$$\frac{d^4 \phi_1(x_1)}{dx_1^4} - \beta_1^4 \phi_1(x_1) = 0 \quad (3)$$

where $\beta_1^4 = \frac{m_1}{E_b I_1} \omega^2$, ω is the natural frequency of the drive

system. The general solution of Eq. (3) can be written as

$$\phi_1(x) = C_1 \sin \beta_1 x + C_2 \cos \beta_1 x + C_3 \sinh \beta_1 x + C_4 \cosh \beta_1 x \quad (4)$$

where C_i ($i=1, 2, 3, 4$) are the coefficients of the modal function determined by boundary conditions. Likewise, the method of solving the modal functions of the transition beam and tentacle is similar with the preceding description. If $\phi_2(x_2)$ represents the modal function of the transition beam, and $\phi_3(x_3)$ represents the modal function of the tentacle, that is

$$\phi_2(x_2) = D_1 \sin \beta_2 x_2 + D_2 \cos \beta_2 x_2 + D_3 \sinh \beta_2 x_2 + D_4 \cosh \beta_2 x_2 \quad (5)$$

$$\phi_3(x_3) = F_1 \sin \beta_3 x_3 + F_2 \cos \beta_3 x_3 + F_3 \sinh \beta_3 x_3 + F_4 \cosh \beta_3 x_3 \quad (6)$$

where D_i and F_i ($i=1, 2, 3, 4$) are the modal function coefficients of the transition beam and tentacle, separately. The parameters

$$\beta_2^4 = \frac{m_2}{E_2 I_2} \omega^2 \text{ and } \beta_3^4 = \frac{m_3}{E_3 I_3} \omega^2, \text{ where } m_2 \text{ and } m_3 \text{ are the mass}$$

per unit length of the transition beam and tentacle. $E_2 I_2$ and $E_3 I_3$ are the bending stiffness of the transition beam and tentacle. The drive system is combined by the piezoelectric beam, transition beam, and tentacle. The modal function coefficient of C_i , D_i , F_i ($i=1, 2, 3, 4$) and natural frequency ω can be determined by the boundary conditions. The specific analysis of the boundary condition is as below:

(1) At the fixed end of the piezoelectric beam, the rotation angle and displacement are equal to 0; At the other end of the piezoelectric beam $x_1=l_1$, the displacement is equal to the displacement of the transition beam at $x_2=0$, and the shear forces at these points ($x_1=l_1$, $x_2=0$) are the action-reaction pair. Thus, the condition can be written as

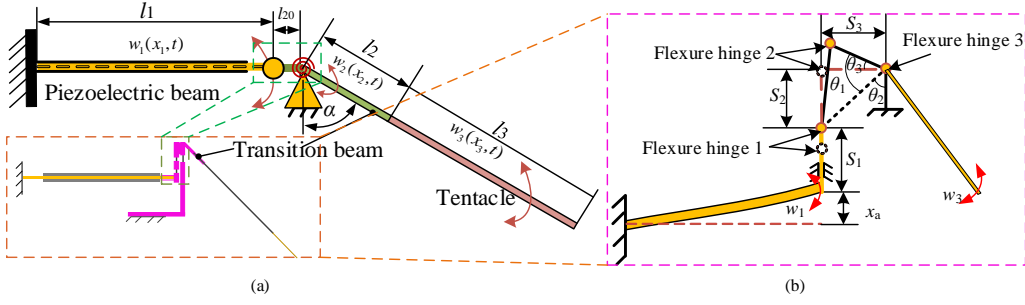


Fig. 3. The simplified physical model for drive system. (a) the simplified physical model; (b) the geometric relationship of the motion.

$$\begin{cases} \phi_1(0) = 0 \\ \phi_1'(0) = 0 \\ \phi_1(l_1) = \phi_2(0) \\ E_b I_1 \phi_1'''(l_1) = -E_2 I_2 \phi_2'''(0) \end{cases} \quad (7)$$

(2) For the point (\$x_2=l_{20}\$) of the transition beam, the displacement is 0 due to the simple supported end; the moment is equal to the moment provided by the flat coil spring. At the coupling point of the transition beam (\$x_2=l_2\$) and the tentacle (\$x_3=0\$), the displacements and rotation angles satisfy the continuity conditions. Thus, the condition can be written as

$$\begin{cases} \phi_2(l_{20}) = 0 \\ -E_2 I_2 \phi_2''(l_{20}) = G \phi_1(l_1)/l_{20} \\ \phi_2'(l_2) = \phi_3'(0) \\ \phi_2(l_2) = \phi_3(0) \end{cases} \quad (8)$$

where \$G\$ is the equivalent rotational stiffness of FMA.

(3) For the tentacle, the moments and shear forces from the tentacle of \$x_3=0\$ and transition beam of \$x_2=l_2\$ are a pair of action and reaction forces separately. Also, the free end of the tentacle has the moment and shear force of 0. Thus, the condition can be written as

$$\begin{cases} E_2 I_2 \phi_2'''(l_2) = -E_3 I_3 \phi_3'''(0) \\ E_2 I_2 \phi_2''(l_2) = -E_3 I_3 \phi_3''(0) \\ \phi_3''(l_3) = 0 \\ \phi_3'''(l_3) = 0 \end{cases} \quad (9)$$

Substituting Eq. (4) – Eq. (5) into the boundary condition Eq. (7)– Eq. (9) and satisfying that the system of equations has non-zero solutions, the modal functions, and natural frequencies can be solved. The modal function of the drive system for the \$i\$-th mode can be expressed as

$$\begin{cases} \phi_1^i(x_1) = C_1^i \sin \beta_1 x_1 + C_2^i \cos \beta_1 x_1 + C_3^i \sinh \beta_1 x_1 + C_4^i \cosh \beta_1 x_1 \\ \phi_2^i(x_2) = D_1^i \sin \beta_2 x_2 + D_2^i \cos \beta_2 x_2 + D_3^i \sinh \beta_2 x_2 + D_4^i \cosh \beta_2 x_2 \\ \phi_3^i(x_3) = F_1^i \sin \beta_3 x_3 + F_2^i \cos \beta_3 x_3 + F_3^i \sinh \beta_3 x_3 + F_4^i \cosh \beta_3 x_3 \end{cases} \quad (10)$$

B. Forced vibration for the drive system without water

The drive power come from the piezoelectric beams and is transferred to the tentacle by the FAM. For the analysis of the forced vibration, the forced response of the piezoelectric beam needs to be solved first. Employing the obtained generalized coordinates, the forced response of the drive system can be calculated according to the boundary condition. The piezoelectric ceramics are attached on the brass beam in a parallel connection. If a sine voltage signal \$V_3 e^{i\omega t}\$ is supplied to the piezoelectric ceramics, the electric field strength can be expressed as

$$E_c(t) = \frac{V_3 e^{i\omega t}}{h_p} \quad (11)$$

where \$V_3\$ is the amplitude of the excitation signal, \$h_p\$ is the thickness of the piezoelectric ceramic sheet. From the piezoelectric equations of stress-charge form, the stress of the piezoelectric ceramic sheet can be obtained as

$$\sigma_p(x_1, t) = -e_{31} E_c + \frac{h}{2} c_{11}^E \frac{\partial^2 w_1(x_1, t)}{\partial x_1^2} \quad (12)$$

where \$e_{31}\$ is the piezoelectric constant, \$c_{11}^E\$ is the stiffness coefficient of the piezoelectric ceramic. Then, the strain energy of the piezoelectric ceramic sheets can be solved as

$$V_p = \frac{Wh}{4} \sum_{i=1}^{\infty} q_1^{(i)}(t) \int_0^{l_1} [-e_{31} E_3 \phi_1^{(i)''}(x_1)] dx_1 + \frac{1}{2} \sum_{i=1}^{\infty} k_{ij}^p q_1^{(i)}(t) q_1^{(j)}(t) \quad (13)$$

where \$q_1(t)\$ is the generalized coordinate, \$W\$ is the width of the piezoelectric beam, \$k_{ij}^p = k_{ji}^p = \int_0^{l_1} \frac{Wh}{4} c_{11}^E \phi_1^{(i)''}(x) \phi_1^{(j)''}(x) dx_1\$. Also,

the strain energy of the brass substrate can be solved as

$$V_c = \frac{1}{2} \sum_{i=1}^{\infty} \sum_{j=1}^{\infty} k_{ij} q_1^{(i)}(t) q_1^{(j)}(t) \quad (14)$$

where \$k_{ij} = k_{ji} = \int_0^{l_1} E_b I_1 \phi_1^{(i)''}(x_1) \phi_1^{(j)''}(x_1) dx_1\$. The total strain energy of the piezoelectric beam is the summation of Eq. (13) and Eq. (14), that is \$V=V_p+V_c\$. For the kinetic energy of the piezoelectric beam, we obtain the form as

$$T = \frac{1}{2} \sum_{i=1}^{\infty} \sum_{j=1}^{\infty} m_{ij} \dot{q}_1^{(i)}(t) \dot{q}_1^{(j)}(t) \quad (15)$$

Considering the damping effect, the dissipation function can be expressed as

$$D = \frac{1}{2} \sum_{i=1}^{\infty} \sum_{j=1}^{\infty} c_{ij} \dot{q}_1^{(i)}(t) \dot{q}_1^{(j)}(t) \quad (16)$$

where \$c_{ij} = c_{ji} = \int_0^{l_1} C \phi_1^i(x) \phi_1^j(x) dx_1\$. Substituting Eq. (13)– Eq. (14) into the Lagrange equation and according to the orthogonality of modes, the forced dynamic equation can be obtained as

$$M^{(i)} \ddot{q}(t) + C^{(i)} \dot{q}(t) + K^{(i)} q(t) = F^{(i)}(t) \quad (17)$$

where \$M^{(i)} = \int_0^{l_1} m_1 \phi_1^{(i)2} dx_1\$ is the modal mass of the \$i\$-th mode,

\$K^{(i)} = \int_0^{l_1} E_b I_1 \phi_1^{(i)''2} dx_1\$ is the modal stiffness of the \$i\$-th mode, \$C^{(i)}\$ is the modal damping, \$F^{(i)}(t)\$ is the generalized forced that can be calculated by

$$F^{(i)}(t) = \frac{Wh}{4} \int_0^{l_1} e_{31} E_c \phi_1^{(i)''}(x_1) dx_1 \quad (18)$$

Using the Duhamel integral, the forced displacement response of the piezoelectric beam can then be solved as

$$w_1(x_1, t) = \sum_{i=1}^{\infty} \frac{O^{(i)} \phi_1^{(i)}(x_1) e^{i(\omega t - \phi^{(i)})}}{K^{(i)} \sqrt{(1-r^2)^2 + (2\zeta^{(i)}r)^2}} \quad (19)$$

where $O^{(i)} = \frac{Whe_{31}}{4h_p} \int_0^4 V_3(x_1) \phi_1^{(i)*}(x_1) dx_1$, $\phi^{(i)} = \arctan(2\zeta^{(i)}r / (1-r^2))$, $\zeta^{(i)}$

is the damping ratio, and r is the frequency ratio. In the term of the drive system, the generalized coordinate $q_1(t)$ is applicable to the whole system. Thus, the forced displacement response of the transition beam and tentacle can be calculated by the boundary conditions (i.e., $w_1(l_1, t) = w_2(l_2, t)$, $w_1(l_2, t) = w_3(0, t)$). The forms of forced displacement response of the transition beam and tentacle can be written as

$$w_2(x_2, t) = \sum_{i=1}^{\infty} \frac{\phi_2^{(i)}(x_2) O^{(i)} \phi_1^{(i)}(l_1) e^{i(\omega t - \phi^{(i)})}}{K^{(i)} \phi_2^{(i)}(0) \sqrt{(1-r^2)^2 + (2\zeta^{(i)}r)^2}} \quad (20)$$

$$w_3(x_3, t) = \sum_{i=1}^{\infty} \frac{\phi_3^{(i)}(x_3) \phi_2^{(i)}(l_2) O^{(i)} \phi_1^{(i)}(l_1) e^{i(\omega t - \phi^{(i)})}}{K^{(i)} \phi_3^{(i)}(0) \phi_2^{(i)}(0) \sqrt{(1-r^2)^2 + (2\zeta^{(i)}r)^2}} \quad (21)$$

C. Forced vibration and propulsion force of the drive system underwater

When the robotic jellyfish are immersed in water, the natural frequency of the drive system would decline due to the inhibitory effect of liquid on the system. Considering the water effect on the beam structure of the drive system, here, the theoretical analysis proposed by Sader et al. [33] for the forced response of a cantilever beam immersed in a viscous fluid is employed to calculate the response of the drive system. The hydrodynamic functions of the beams are given by

$$\Gamma(\text{Re}) = \Omega(\text{Re}) \left[1 + \frac{4jK_1(-j\sqrt{j\text{Re}})}{\sqrt{j\text{Re}K_0(-j\sqrt{j\text{Re}})}} \right] \quad (22)$$

where $\text{Re} = \rho_w \omega W_i / (4\eta)$ is the Reynolds number in which ρ_w and η are the density and viscosity of the fluid, respectively, W_i ($i=1, 2, 3$) is the beam width of the subsystem, the functions K_0 and K_1 are modified Bessel functions of the third kind, $\Omega(\text{Re})$ is the correction function [33]. For the sub-beams of the drive system underwater, the external applied load $F_i(x_i, \omega)$ can be separated into two components, that is, $F_{\text{hydro}}(x_i, \omega)$ caused by the motion of the fluid around the beam and $F_{\text{drive}}(x_i, \omega)$ the excitation force which can be calculated by Eq. (18). Thus, the force of the drive system can be written as

$$\begin{cases} F_1(x_1, \omega) = F_{\text{drive}}(x_1, \omega) + F_{\text{hydro}}(x_1, \omega) \\ F_2(x_2, \omega) = F_{\text{hydro}}(x_2, \omega) \\ F_3(x_3, \omega) = F_{\text{hydro}}(x_3, \omega) \end{cases} \quad (23)$$

where $F_{\text{hydro}}(x_i, \omega) = \frac{\pi}{4} \rho_w \omega^2 \Gamma(\omega) W_i^2 w_{i,\text{water}}(x_i, \omega)$, w_i is the displacement response of the sub-systems underwater. Substituting Eq. (23) into the frequency domain form of Eq. (1) and rearranging the equation, we find the equivalent mass of the drive system and equivalent damping ratio underwater that can be expressed as

$$m_i^t = m_i + m_i^a \quad (24)$$

$$\zeta_i^t = \zeta + \sum_{i=1}^3 \zeta_i^h \quad (25)$$

where m_i^a is the added mass per length, $m_i^a = \frac{\pi \rho W_i^2}{4} \Gamma_r$, ζ_i^h is the hydrodynamic damping ratio, $\zeta_i^h = \Gamma_i / 2(\frac{4m_i}{\pi \rho W_i^2} + \Gamma_r)$, in which Γ_r and Γ_i are the real and imaginary parts of the hydrodynamic function Γ . Substituting Eq. (24) into the boundary conditions of Eq. (7)- Eq. (9), the modal functions of the drive system underwater can be solved which is denoted as $\phi_{j,\text{water}}^{(i)}(x_j)$ ($j=1, 2, 3$). Furthermore, substituting Eq. (24) and Eq. (25) into the Eq. (17), the solutions to the displacement response $w_{i,\text{water}}$ of the subsystem underwater can be obtained. The swimming of the jellyfish depends on the swing of the tentacles. When the forced responses of the tentacles underwater are obtained, the mean thrust in water is given in Lighthill's theory [34] as

$$T = \frac{1}{2} m_v \left[\left(\frac{\partial w_{3,\text{water}}}{\partial t} \right) - U^2 \left(\frac{\partial w_{3,\text{water}}}{\partial x_3} \right)^2 \right]_{x_3=l_3} \quad (26)$$

where U is an external relative free stream speed, m_v is the virtual mass density at the end of the tentacle, expressed as

$m_v = \frac{\pi \rho_w W_3^2}{4} \delta$, δ is a virtual mass coefficient that is close to unity [33, 35]. In addition, if the jellyfish is in quiescent water, the speed U is set to 0. Thus, the thrust of Eq. (26) reduces as

$$T = \frac{1}{2} m_v \left(\frac{\partial w_{3,\text{water}}}{\partial t} \right)_{x=l_3}^2 = \frac{\pi \rho_w W_3^2}{8} \left(\frac{\partial w_{3,\text{water}}(l_3, t)}{\partial t} \right)^2 \quad (27)$$

However, the preceding solved the thrust T along the length of the tentacles, since the tentacles are evenly arranged on the circumference and form a certain angle with the vertical direction as shown in Fig. 2(c), where the resultant vertical force component of each tentacle is the propulsion force. Therefore, the propulsion force of the robotic jellyfish under the excitation can be expressed as

$$T_{\text{lift}} = nT \cos(\alpha + \theta_3(t)) \quad (28)$$

where n is the number of tentacles, α is the angle between the tentacles and the vertical direction, and $\theta_3(t)$ is the relative angle of the swing.

D. Results analysis and discussion

To investigate the inherent and dynamic characteristics of the drive system, the design parameters for the robotic jellyfish configuration provided in Table 1 and Table 3 are substituted into the corresponding equations for numerical calculation. The first-four modes and natural frequencies of the drive system in the case of underwater and without water are obtained as shown in Fig. 4 and Fig. 5. From Fig. 4, the first four natural frequencies of the drive system underwater are 2.89 Hz, 37.54 Hz, 87.94 Hz, and 232.86 Hz. Compared with the case of that

TABLE I
The Parameters of the Piezoelectric Beam.

Quantities	Values	Quantities	Values
l_1	45 mm	l_p	40 mm
h_1	0.4 mm	h_p	0.23 mm
W_1	10 mm	W_p	10 mm
E_b	105 GPa	E_p	76.5 GPa
ρ_b	8500 kg/m ³	ρ_p	7500 kg/m ³
$E_b I_1$	$2.46 \times 10^{-2} \text{ Nm}^2$	e_{31}	5.5 C/m ²

TABLE II
The Parameters of the Transition Beam and Tentacle.

Transition beam		Tentacle	
Quantities	Values	Quantities	Values
l_2	13 mm	l_3	55 mm
h_2	1.5 mm	h_3	0.2 mm
W_2	5 mm	W_3	10 mm
E_2	3.5 GPa	E_3	15 GPa
ρ_2	1200 kg/m ³	ρ_3	1500 kg/m ³
G	1.3×10^{-2} Nm/rad	α	60°
$E_2 I_2$	1.4×10^{-2} Nm ²	$E_3 I_3$	1×10^{-4} Nm ²
l_{20}	2 mm		

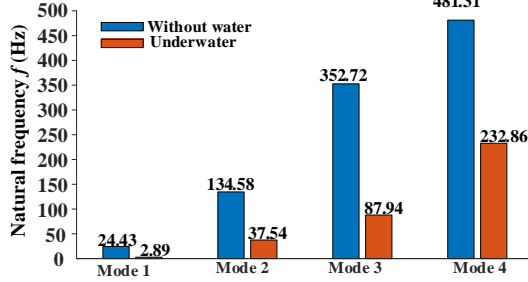


Fig. 4. The first-four order natural frequencies of the drive system. without water, each natural frequency mode has declined by 89%, 72%, 75%, and 52%, respectively. The first-order natural frequency decreases the most, but with the increase of the mode order, the rate of decline gradually decreased, showing that the influence of added mass and added damping caused by the water environment on the driving system becomes weaker.

Fig. 5 shows the comparison of the vibration shapes in the two cases, key findings emerge:

(1) Among the first four order modes, the vibration shapes of mode 1 in the two cases are almost consistent. With the increase of the mode order, the vibration shapes of the piezoelectric beam and tentacles diverge, and the different response of the tentacles is more significant, while, the change of the vibration shapes of the transition beam is not so obvious.

(2) For the tentacle, the underwater vibration shapes exhibit more peaks and troughs compared to that without water in the high-order modes. In the first-four underwater order modes, the maximum displacement responses of the piezoelectric beam occur at the end except for the third-order mode. The deformations of the transition beam are small in the two cases, so the power can be transferred from the piezoelectric beam to the tentacle which also is our design purpose.

(3) To create a greater propulsion force, a larger swing amplitude of the tentacle is desired. The power input end is the end of the piezoelectric beam, and the power output end is the free end of the tentacle. The larger the vibration amplitude ratio of these two positions, the better the propulsion performance of

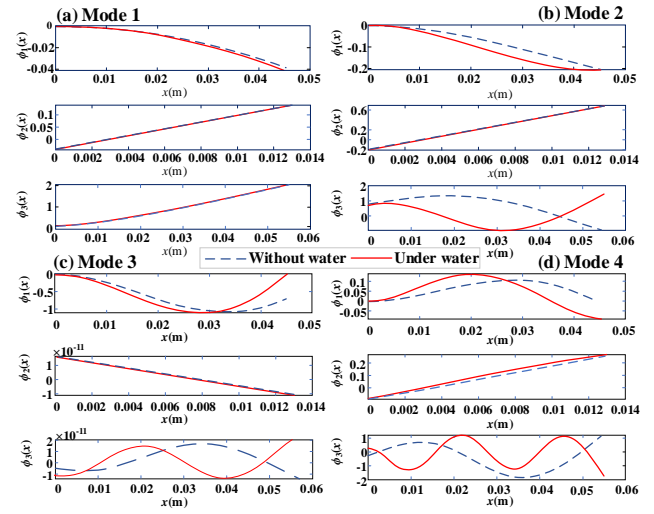


Fig. 5. The modal function of drive system in case of without water and underwater. (a) mode 1; (b) mode 2; (c) mode 3; (d) mode 4.

the robot. In the first-four order modes, the vibration amplitude ratios are 49.88, 9.99, 6.37, and 1.77, respectively. Thus, the first mode is the most suitable working mode for the robotic jellyfish.

The lift is the key item for the swimming of the robotic jellyfish. Different configurations of installation angle α , beam width W_3 , and tentacle number are investigated for the effect on the lift. Fig. 6 presents the lift curves with different configuration parameters in one motion cycle. From Fig. 6, key findings emerge:

(1) The lift in one motion cycle is fluctuating. If the installation angle of the tentacle is too large (75° and 90°), parts of the lift curve would have negative values. As the installation angle increases, the area covered by the curve on the positive and negative half axes gradually approaches. At this time, the jellyfish will not perform the swimming motion. All parts of the lift curve being at the positive axes of the coordinate system is desired for the design, so the installation angle is allowed to be less than or equal to 60°.

(2) If the installation angle of the tentacle is set as 60°, which ensures that the tentacles swing without contacting the body and tank bottom, from Fig. 6(b), the tentacle with a larger width can obtain greater lift. The maximum instantaneous lift can reach 0.35 mN with a tentacle width of 12 mm. Thus, a wider tentacle can be appropriately used in the experimental prototype.

(3) Moreover, From Fig. 6(c), The application of more tentacles will contribute more lift to improve the swimming speed. However, the number of tentacles will not exceed four. Too many tentacles can increase the longitudinal dimension and are hard to arrange in the circumferential direction.

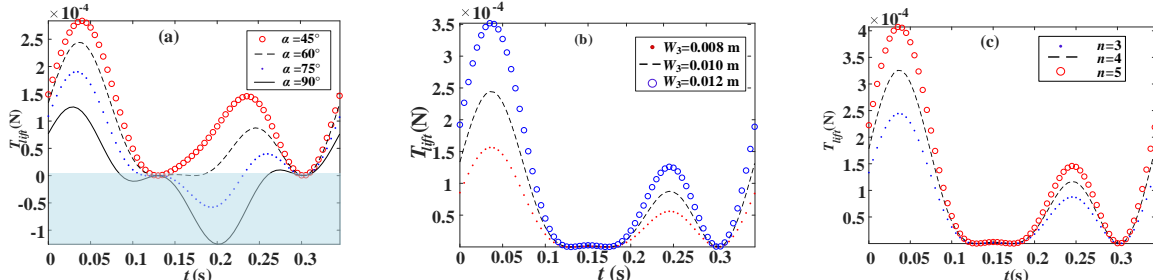


Fig. 6. The lift of the robotic jellyfish with different configurations. (a) different installation angles; (b) different beam widths; (c) different tentacle numbers.

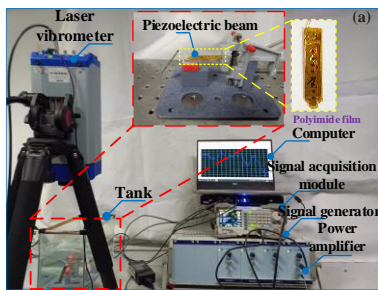


Fig. 7. The experimental setup for the dynamic characteristics of the drive system.

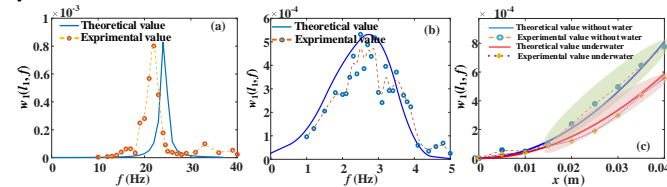


Fig. 8. The dynamic characteristics of the piezoelectric beam: (a) amplitude-frequency characteristics without water; (b) amplitude-frequency characteristics underwater (c) the vibration shape of the piezoelectric beam.

IV. EXPERIMENTS

To verify the correctness of the theoretical analysis, the dynamic characteristics of the drive system are measured underwater and without water. The swimming performance identification of the proposed robotic jellyfish with the change of the drive signal frequency is also carried out. To facilitate the test, the working mode of the piezoelectric beam is measured as the target of verification. The voltage amplitude of the drive signal power amplifier supplying the piezoelectric beam was 100 V. Waterproof measures for the piezoelectric beams must be considered before being tested in water. Various materials such as plastic film encapsulation, waterproof coatings, and polyimide films were investigated. After testing these, it was found the polyimide films could provide a long-term solution for use in the submerged robot jellyfish. The displacement responses were collected by laser vibrometer and signal acquisition module, and the data were processed and visualized by the computer as shown in Fig. 7. The sweep frequency test was used to find the resonant frequency of the working mode in the cases of without water and underwater, and the sweep frequency interval was set according to the analysis results. The amplitude-frequency characteristics of the piezoelectric beam end without water and underwater are presented in Fig. 8(a) and (b). From Fig. 8(a), the resonant frequency of the piezoelectric beam in the case without water was 23.15 Hz by sweep frequency test which is slightly less than the theoretical value of 24.43 Hz. The deviation is only 5.24%, which may be caused

by ignoring the waterproof measures in the theoretical calculation and possible unstable fixation in the experiment. For the test underwater (see Fig. 8(b)), the resonant frequency of the piezoelectric beam was almost consistent with theoretical value of 2.9 Hz. However, in the experiment, the data tested in the peak area of frequency domain response fluctuated, which can be attributed to the slight flow of water. Moreover, nine test points in the piezoelectric beam were selected for the vibration displacement test, and the measured data are fitted to its vibration form as shown in Fig. 8(c). The displacement response of the whole piezoelectric beam underwater was less than that in the environment without water. The displacement difference at the output end reached 0.21 mm, showing that the experimental vibration modes are in good agreement with the theoretical modes. Thus, the correctness of the theoretical calculation of the working mode of bionic jellyfish is verified.

The assembled jellyfish robot with three tentacles at of installation angle 60° was placed in the water and a balloon was used to buoyancy balance. The drive signal frequency was set to 2.9 Hz. The robotic jellyfish with a rectangle tentacle swam a short distance as shown in Fig. 9(a). The swimming posture of jellyfish represented one rise and one drop, and the swimming distance was 10 mm in 20 s. This shows that the lift provided by the rectangular tentacles was insufficient. Theoretical analysis shows that increasing the width of the tentacles can improve the propulsion ability of the robotic jellyfish. So, the rectangle tentacles were improved to fin-like tentacles, and the water-pushing area of the tentacle was increased. The improved robotic jellyfish presented a better swimming ability in the underwater experiments which achieved an upward climb at the drive frequency of 0.4-1.6 Hz. As the width of the tentacles increasing, the damping effect on the tentacles would increase, and the optimal driving frequency decreases. Fig. 9(b) presents the swimming distance with a drive frequency range of 0.4-1.2 Hz. The curves show the robotic jellyfish swims slowly in the start-up phase, and then shows an accelerated state. Among them, for the same time, the robotic jellyfish with an excitation frequency of 0.8 Hz has the largest swimming distance and that with an excitation frequency of 0.4 Hz has the shortest swimming distance. Fig. 9(c) presents the average speed of the robotic jellyfish with the change of drive frequency. From Fig. 9(c), the optimal operating frequency for the robotic jellyfish was 0.7-1.1 Hz. The maximum swimming speed was 10 mm/s at a drive frequency of 0.8 Hz. This also shows that the change in tentacle form reduced the natural frequencies of the working modes of the drive system.

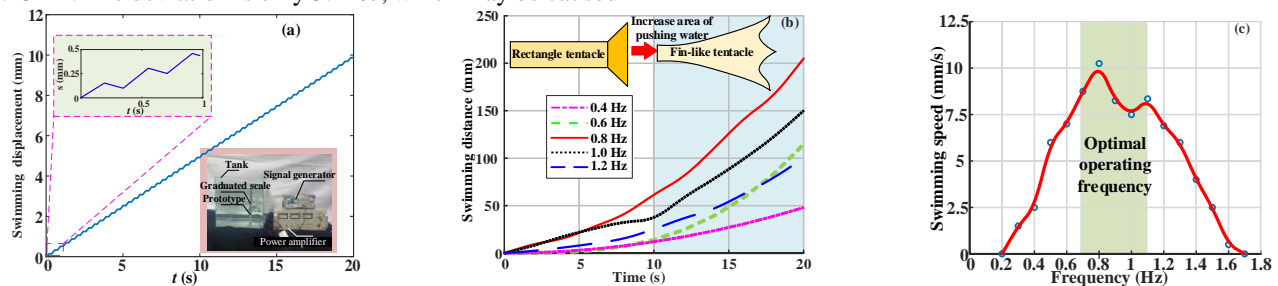


Fig. 9. Swimming test for the robotic jellyfish underwater. (a) the swimming test with rectangle tentacle; (b) the swimming test with fin-like tentacle; (c) the average speed with the change of drive frequency.

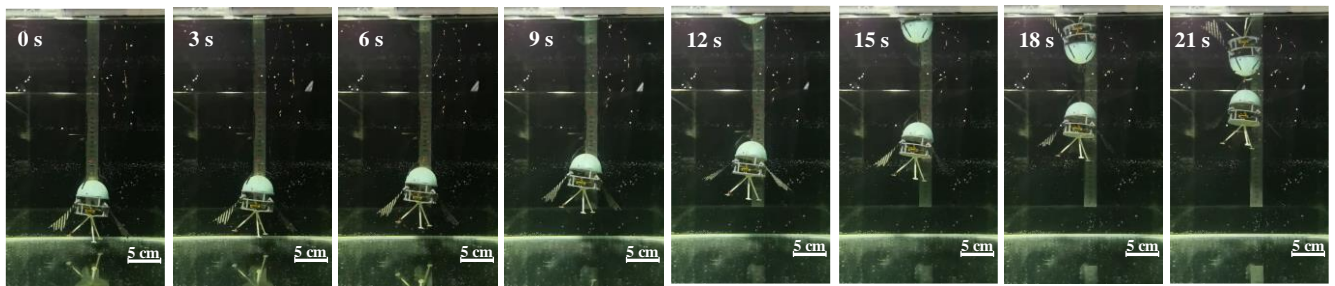


Fig. 10. Swimming demonstration of the robotic jellyfish.

TABLE III.
COMPARISON OF THE ROBOTIC JELLYFISH ACTUATED BY SMART MATERIALS IN THE LITERATURE.

Paper	Actuator	Wireless controllability	Voltage (V) /Current (A)	Frequency (Hz)	Weight (g)	Bell Diameter (mm)	Speed (mm/s)
Cheng et al. [19]	DE	Yes	7000-900 V	1.6	28	156	10
Wang et al. [23]	DE	No	5000 V	2	100	240	5
Ko et al. [16]	EMA	Yes	13 A	10	0.14	17	–
Barbar et al. [21]	IPMC	No	2 V	3.5	–	165	2
Mohamad et al. [11]	SMA spring	No	18 V	0.5	40.1	76	20
Almubarak et al. [14]	SMA	No	12 V	0.33	650	210	60
Zhou et al [36]	PZT	No	300 V	250	54	109	28
This paper	PZT	No	100 V	0.8	29.5	150	10

“–” indicates that the information is not available.

Fig. 10 presents a demonstration of the robotic jellyfish operation with a drive voltage of 100 V and a drive frequency of 0.8 Hz. The swimming distances were recorded every 3 s. The operating state of the robotic jellyfish shows that it swims slowly in the starting phase, then accelerates up, and then maintains a steady swimming phase. When the bionic jellyfish swims vertically, the average swimming speed of the bionic jellyfish can reach 10 mm/s.

Table III shows a comparison for the state-of-the-art jellyfish-like swimming robots actuated by smart materials. The highlights of this work can be summarized as

(1) Due to the fast response of piezoelectric materials, Piezo-driven robotic jellyfish can possess swimming frequencies that are closer to those of real jellyfish, and the swimming frequency can be controlled by the dimensions of the proposed FMA.

(2) The drive voltage for the proposed robotic jellyfish is moderate. It is beneficial for the electromechanical integration of cableless designs in further research. The compact structure design allows the robot jellyfish to have a transmission mechanism while maintaining a light weight.

(3) Reference [36] describes an underwater robot driven by piezoelectric actuators that achieves multi-locomotion mode, high agility and maneuverability. However, this underwater robot with six piezoelectric drive units has a speed of 28 mm/s at a drive voltage of 300 V and a drive frequency of 250 Hz. Compared to the robotic jellyfish proposed in this paper, it has 3 times the drive voltage and 312 times the drive frequency, yet has a speed of only 2.8 times of the proposed robotic jellyfish. Therefore, mimicking natural creature swimming motion is a higher efficient way.

V. CONCLUSIONS AND PERSPECTIVES

The innovation and novelty in this paper involve the piezoelectric beam actuator under low drive frequency were applied to drive a bionic robotic jellyfish; a new type of large deformation composite flexure hinge was developed; the manufacturing process of the flexure hinge was released; the multi-continuum coupled dynamic equations of the drive

system are established to calculate and investigate the lift of the robotic jellyfish. The correctness of the theoretical analysis was verified by the experiments. The experiments for testing the dynamic characteristics and swimming performance showed that the robotic jellyfish has an optimal average swimming speed of 10 mm/s with a drive voltage of 100 V and a drive frequency of 0.8 Hz.

Future work involves improving the structure and manufacturing process, developing the control strategies and electromechanical integration of cableless designs, and completing the design theory for the proposed flexure hinge. Moreover, we will develop potential applications of the robotic jellyfish in water quality testing and marine species biological data collection. We also hope the results provide a basis to inspire many researchers to further develop micro soft robots with piezoelectric actuators.

REFERENCES

- [1] J. Yu, C. Zhang, and L. Liu, “Design and Control of a Single-Motor-Actuated Robotic Fish Capable of Fast Swimming and Maneuverability,” *IEEE/ASME Transactions on Mechatronics*, vol. 21, no. 3, pp. 1711–1719, Jun. 2016, doi: 10.1109/tmech.2016.2517931.
- [2] X. Hu, Z. Ge, X. Wang, N. Jiao, S. Tung, and L. Liu, “Multifunctional thermo-magnetically actuated hybrid soft millirobot based on 4D printing,” *Composites Part B: Engineering*, vol. 228, p. 109451, Jan. 2022, doi: 10.1016/j.compositesb.2021.109451.
- [3] Z. Ying, H. Zhang, L. Wang, and R. Melnik, “Propulsion optimization of a jellyfish-inspired robot based on a nonintrusive reduced-order model with proper orthogonal decomposition,” *Bioinspiration & Biomimetics*, vol. 17, no. 4, p. 046005, May 2022, doi: 10.1088/1748-3190/ac6374.
- [4] J. Xiao, J. Duan, and J. Yu, “Design and implementation of a novel biomimetic robotic jellyfish,” in *2013 IEEE International Conference on Robotics and Biomimetics (ROBIO)*, 2013. Available: <http://dx.doi.org/10.1109/robio.2013.6739592>.
- [5] J. Frame, N. Lopez, O. Curet, and E. D. Engeberg, “Thrust force characterization of free-swimming soft robotic jellyfish,” *Bioinspiration & Biomimetics*, vol. 13, no. 6, p. 064001, Sep. 2018, doi: 10.1088/1748-3190/aadcb3.
- [6] P. Liao, S. Zhang, and D. Sun, “A dual caudal-fin miniature robotic fish with an integrated oscillation and jet propulsive mechanism,” *Bioinspiration & Biomimetics*, vol. 13, no. 3, p. 036007, Mar. 2018, doi: 10.1088/1748-3190/aaa9cc.

- [7] G. Bridges, M. Raach, and M. F. Stoelen, "Jellyfish Inspired Soft Robot Prototype Which Uses Circumferential Contraction for Jet Propulsion," in *Biomimetic and Biohybrid Systems*, Cham: Springer International Publishing, 2017, pp. 61–72. Available: http://dx.doi.org/10.1007/978-3-319-63537-8_6.
- [8] Z. Lin, T. Jiang, and J. Shang, "The emerging technology of biohybrid micro-robots: a review," *Bio-Design and Manufacturing*, vol. 5, no. 1, pp. 107–132, May 2021, doi: 10.1007/s42242-021-00135-6.
- [9] Y. Hao, S. Zhang, B. Fang, F. Sun, H. Liu, and H. Li, "A Review of Smart Materials for the Boost of Soft Actuators, Soft Sensors, and Robotics Applications," *Chinese Journal of Mechanical Engineering*, vol. 35, no. 1, Apr. 2022, doi: 10.1186/s10033-022-00707-2.
- [10] Z. Wang, G. Hang, J. Li, Y. Wang, and K. Xiao, "A micro-robot fish with embedded SMA wire actuated flexible biomimetic fin," *Sensors and Actuators A: Physical*, vol. 144, no. 2, pp. 354–360, Jun. 2008, doi: 10.1016/j.sna.2008.02.013.
- [11] M. A. Kazemi Lari, A. D. Dostine, J. Zhang, A. S. Wineman, and J. A. Shaw, "Robotic jellyfish actuated with a shape memory alloy spring," in *Bioinspiration, Biomimetics, and Bioreplication IX*, 2019. Available: <http://dx.doi.org/10.1117/12.2513456>.
- [12] A. Hamidi, Y. Almubarak, Y. M. Rupawat, J. Warren, and Y. Tadesse, "Poly-Saora robotic jellyfish: swimming underwater by twisted and coiled polymer actuators," *Smart Materials and Structures*, vol. 29, no. 4, p. 045039, Mar. 2020, doi: 10.1088/1361-665x/ab7738.
- [13] A. Villanueva, C. Smith, and S. Priya, "A biomimetic robotic jellyfish (RoboJelly) actuated by shape memory alloy composite actuators," *Bioinspiration & Biomimetics*, vol. 6, no. 3, p. 036004, Aug. 2011, doi: 10.1088/1748-3182/6/3/036004.
- [14] Y. Almubarak, M. Punnoose, N. X. Maly, A. Hamidi, and Y. Tadesse, "KryptoJelly: a jellyfish robot with confined, adjustable pre-stress, and easily replaceable shape memory alloy NiTi actuators," *Smart Materials and Structures*, vol. 29, no. 7, p. 075011, Jun. 2020, doi: 10.1088/1361-665x/ab859d.
- [15] F. Kong, Y. Zhu, C. Yang, H. Jin, J. Zhao and H. Cai, "Integrated Locomotion and Deformation of a Magnetic Soft Robot: Modeling, Control, and Experiments," in *IEEE Transactions on Industrial Electronics*, vol. 68, no. 6, pp. 5078–5087, June 2021, doi: 10.1109/TIE.2020.2992000.
- [16] Y. Ko et al., "A jellyfish-like swimming mini-robot actuated by an electromagnet actuation system," *Smart Materials and Structures*, vol. 21, no. 5, p. 057001, Apr. 2012, doi: 10.1088/0964-1726/21/5/057001.
- [17] Z. Ren, W. Hu, X. Dong, and M. Sitti, "Multi-functional soft-bodied jellyfish-like swimming," *Nature Communications*, vol. 10, no. 1, Jul. 2019, doi: 10.1038/s41467-019-10549-7.
- [18] R. K. Jain, "Application of Ionic Polymer Metal Composite (IPMC) as Soft Actuators in Robotics and Bio-Mimetics," in *Ionic Polymer–Metal Composites*, Boca Raton: CRC Press, 2022, pp. 53–94. Available: <http://dx.doi.org/10.1201/9781003204664-4>.
- [19] T. Cheng, G. Li, Y. Liang, et al., "Untethered soft robotic jellyfish," *Smart Materials and Structures*, vol. 28, no. 1, pp.015019, Nov. 2018, doi: 10.1088/1361-665x/aaed4f.
- [20] S. Chen et al., "Soft Crawling Robots: Design, Actuation, and Locomotion," *Advanced Materials Technologies*, vol. 5, no. 2, p. 1900837, Dec. 2019, doi: 10.1002/admt.201900837.
- [21] B. Akle, J. Najem, D. Leo, and J. Blottman, "Design and development of bio-inspired underwater jellyfish like robot using ionic polymer metal composite (IPMC) actuators," in *SPIE Proceedings*, 2011. Available: <http://dx.doi.org/10.1117/12.881993>.
- [22] Z. Chen, T. I. Um, and H. Bart-Smith, "A novel fabrication of ionic polymer–metal composite membrane actuator capable of 3-dimensional kinematic motions," *Sensors and Actuators A: Physical*, vol. 168, no. 1, pp. 131–139, Jul. 2011, doi: 10.1016/j.sna.2011.02.034.
- [23] S. Wang and Z. Chen, "Modeling of jellyfish-inspired robot enabled by dielectric elastomer," *International Journal of Intelligent Robotics and Applications*, vol. 5, no. 3, pp. 287–299, Aug. 2021, doi: 10.1007/s41315-021-00192-1.
- [24] C. Christianson et al., "Jellyfish-Inspired Soft Robot Driven by Fluid Electrode Dielectric Organic Robotic Actuators," *Frontiers in Robotics and AI*, vol. 6, Nov. 2019, doi: 10.3389/frobt.2019.00126.
- [25] Q. Zhang, W. Chen, Y. Liu, J. Liu, and Q. Jiang, "A Frog-Shaped Linear Piezoelectric Actuator Using First-Order Longitudinal Vibration Mode," *IEEE Transactions on Industrial Electronics*, vol. 64, no. 3, pp. 2188–2195, Mar. 2017, doi: 10.1109/tie.2016.2626242.
- [26] J. Li, Y. Liu, J. Deng, S. Zhang, and W. Chen, "Development of a Linear Piezoelectric Microactuator Inspired by the Hollowing Art," *IEEE Transactions on Industrial Electronics*, vol. 69, no. 10, pp. 10407–10416, Oct. 2022, doi: 10.1109/tie.2022.3152008.
- [27] J. Pan, Z. Zhou, J. Wang, P. Zhang and J. Yu, "Development of a Penguin-Inspired Swimming Robot with Air Lubrication System," in *IEEE Transactions on Industrial Electronics*, doi: 10.1109/TIE.2022.3172753.
- [28] J. Li, H. Huang, and H. Zhao, "A Piezoelectric-Driven Linear Actuator by Means of Coupling Motion," *IEEE Transactions on Industrial Electronics*, vol. 65, no. 3, pp. 2458–2466, Mar. 2018, doi: 10.1109/tie.2017.2740828.
- [29] A. Alejandre, O. Olszewski, and N. Jackson, "Actuation control of a PiezoMEMS biomimetic robotic jellyfish," in *SPIE Proceedings*, 2017. Available: <http://dx.doi.org/10.1117/12.2264605>.
- [30] Y. Chen et al., "A biologically inspired, flapping-wing, hybrid aerial-aquatic microrobot," *Science Robotics*, vol. 2, no. 11, Oct. 2017, doi: 10.1126/scirobotics.aao5619.
- [31] H. McClintock, F. Z. Temel, N. Doshi, J. Koh, and R. J. Wood, "The milliDelta: A high-bandwidth, high-precision, millimeter-scale Delta robot," *Science Robotics*, vol. 3, no. 14, Jan. 2018, doi: 10.1126/scirobotics.aar3018.
- [32] C. P. Green and J. E. Sader, "Frequency response of cantilever beams immersed in viscous fluids near a solid surface with applications to the atomic force microscope," *Journal of Applied Physics*, vol. 98, no. 11, p. 114913, Dec. 2005, doi: 10.1063/1.2136418.
- [33] C. A. Van Eysden and J. E. Sader, "Frequency response of cantilever beams immersed in compressible fluids with applications to the atomic force microscope," *Journal of Applied Physics*, vol. 106, no. 9, p. 094904, Nov. 2009, doi: 10.1063/1.3254191.
- [34] M. J. Lighthill, "Aquatic animal propulsion of high hydromechanical efficiency," *Journal of Fluid Mechanics*, vol. 44, no. 02, p. 265, Nov. 1970, doi: 10.1017/s0022112070001830.
- [35] M. J. Lighthill, "Large-amplitude elongated-body theory of fish locomotion," *Proceedings of the Royal Society of London. Series B. Biological Sciences*, vol. 179, no. 1055, pp. 125–138, Nov. 1971, doi: 10.1098/rspb.1971.0085.
- [36] X. Zhou, K. Li, Y. Liu, et al. Development of an anti-hydropressure miniature underwater robot with multi-locomotion mode using piezoelectric pulsed-jet actuator, *IEEE Transactions on Industrial Electronics*, 2022, doi: 10.1109/TIE.2022.3189088.

Biographical notes



Jichun Xing (M'18) was born in Liaoning, China, in 1983. He received the B.S. degree in mechanical design, manufacturing and automation from Liaoning University of Technology, Jinzhou, China, in 2006 and the Ph.D. degree in mechanical design and theory from Yanshan University, Qinhuangdao, China, in 2012. He was a Visiting Scholar at the School of Civil and Mechanical Engineering, Curtin University, Perth, Australia, from July 2019 to August 2020. He is currently an Associate Professor with Yanshan University, Qinhuangdao, China. His current research interests include piezoelectric drive and control technology.



Wei Jin was born in Shanxi, China in 1995. He received the B.S. degree in mechanical design, manufacturing and automation from Jimusi University, Jimusi, China, in 2019. He is currently pursuing the Master degree in mechanical design and theory in Yanshan University, Qinhuangdao, China. His current research interests include piezoelectric drive and control technology.



Kuang Yang was born in Hebei, China in 1996. He received the B.S. degree in mechanical design, manufacturing and automation from Guilin University of Electronic Technology, Guilin, China, in 2020. He is currently pursuing the Master degree in mechanical design and theory in Yanshan university, Qinhuangdao, China. His current research interests include piezoelectric drive and control technology.



Ian Howard was born in Perth, Australia, in 1962. He received the B.S. degree and Ph.D. degree in mechanical engineering from University of Western Australia, Australia, in 1983 and 1988 respectively. He is currently an Emeritus Professor with Curtin University, Perth, Australia. His current research interests include dynamic modelling, vibration power harvesting, and gear dynamics.